RESEARCH PAPER

Space confinement of physical deposited Au nanoparticles on a three-dimensional-branched TiO$_2$ photoanode for efficient photoelectrochemical overall water splitting

Chen Cui · Tingyu Chen · Huiju Huang ·
Zhushuo Li · Fengjiao Yu · Jun Fang ·
Yang Yang

Abstract In this paper, we present an effective route for boosting the photoelectrochemical overall water splitting to produce hydrogen and oxygen by modified TiO$_2$ nanowire arrays (NWAs) photoanode. Such modification includes the synthesis of branched TiO$_2$ NWAs and followed by the deposition of Au nanoparticles (NPs) via the magnetron sputtering and post-annealing for the dewetting of Au films. The physical deposition of Au on the TiO$_2$ substrate with a hierarchical structure provides a feasible strategy to produce metal NPs with uniform size and distribution by the space confinement of the branched TiO$_2$ NWAs. Those Au NPs rendered the intensified visible light absorption in a narrow band region due to the surface plasmon resonance (SPR) effect. The amplified electromagnetic field through the SPR excitation of the Au NPs and their passivation upon the surface of TiO$_2$ NWAs led to the efficient generation and transfer of charge carriers. The synergistic effect between branched TiO$_2$ NWAs and Au NPs resulted in the drastic enhancement of the photoelectrochemical overall water splitting to produce hydrogen and oxygen in the stoichiometric ratio. This work provides a facile method for the preparation of hierarchical metal/semiconductor composite photoelectrode with great potential in the efficient photoelectrochemical water splitting for hydrogen energy production and other applications in solar energy conversion.

Keywords Space confinement · Au-decorated TiO$_2$ · Branched nanowire arrays · Photoelectrocatalysis · Overall water splitting

C. Cui · T. Chen · H. Huang · Z. Li · F. Yu · J. Fang (✉) ·
Y. Yang (✉)
State Key Laboratory of Materials-Oriented Chemical Engineering, College of Chemical Engineering, Nanjing Tech University, No. 30 Puzhu South Road, Nanjing 211816, People's Republic of China
e-mail: fangjun@njtech.edu.cn

Y. Yang
e-mail: yangy@njtech.edu.cn

Introduction

Photoelectrochemical (PEC) overall water splitting is widely regarded as one of the promising routes to produce hydrogen as the potential strategy for solar energy conversion [1–12]. It is a green technology aiming to solve the environmental and energy crisis lying in human society [7, 13–16]. Semiconductor materials are an indispensable part as catalysts for boosting the performance of photoelectrochemical devices [15, 17–19]. Due to its low cost, non-toxicity, good photocorrosion resistance, and superior chemical stability, titanium dioxide (TiO$_2$) is considered the most representative n-type semiconductor material for solar energy conversion [9, 16, 20–23]. Since TiO$_2$ was used as a PEC material for water splitting

to produce hydrogen by Fujishima et al. in 1972, it has aroused extensive research interest [24, 25]. However, the application of TiO_2 in photoelectrochemical water splitting is limited by its wide band gap (3.2 eV for anatase and 3.0 eV for rutile), low electron mobility, and high recombination rate of photogenerated electron–hole pairs [10, 12, 13, 26, 27]. One-dimensional nanostructures with directional charge transport channels and shorter charge transport and diffusion lengths can facilitate charge separation [1, 21, 28–30]. However, the one-dimensional (1D) nanostructures of photocatalytic materials still exhibit low efficiency due to the limited surface area and poor light harvesting capability [21, 31]. The synthesis of three-dimensional (3D) hierarchical nanostructures has been proven to be an effective method to improve the performance of photoelectrochemical water splitting, which could effectively overcome the above obstacles. Indeed, this method provides enhanced light absorption, larger specific surface area, efficient charge separation, and carrier mobility [31]. Zheng et al. have synthesized a branched TiO_2 nanorods structure. They showed that the photocurrent increased to 0.83 mA cm^{-2} at 0.8 V vs. RHE, nearly twice higher than the pristine TiO_2 nanorods [32]. Yang et al. have reported a 3D nanostructure of TiO_2 NWAs combined with FeO_x nanoparticles and conducting polymer (CP) network, such hierarchical nanostructure exhibited a significantly enhanced PEC water splitting performance, with the faraday efficiency of 99% for hydrogen production [31].

However, to date, it is still a great challenge for the H_2 and O_2 production from photocatalytic overall pure water splitting, without using any sacrificial agents [25]. Due to the thermodynamic and kinetic limitations, there are only a few candidate materials that could catalyze both the water redox reactions simultaneously and effectively [23, 25, 33–35]. According to previous reports and recent work of our group, the cocatalysts are needed to further enhance the functional PEC properties of TiO_2 NWAs, and noble metals are one of those important candidates. Among those noble metals, Au was extensively studied [36–38]. It is generally acknowledged that the incorporation of Au nanoparticles (NPs) with TiO_2 photocatalysts would greatly enhance electron mobility and maximize light utilization, which could achieve by the Schottky junctions formed between Au NPs and TiO_2 or the surface plasmon resonance

(SPR) effect of Au NPs [39–42]. Basically, the improved PEC properties are built on the fine nanostructure of the electrodes. The size and morphology control of Au NPs nowadays are extensively studied yet need further effort. For example, in the preparation of Au NPs by conventional chemical routes (e.g., chemical reduction of $HAuCl_4$), adding a structural directing agent (polymers in general) would usually lead to the designed morphology of the NPs with fine nanostructure, but it would involve complicated redox process and was not easy to scale up for mass production [43, 44]. Instead, physical deposition of Au (e.g., thermal evaporation, magnetron sputtering, etc.) would be facile and effective for large-scale production, which was generally adopted [45, 46]. Nevertheless, fine control of the morphology of each particle during its dewetting process is another challenging issue on an undefined substrate [47, 48]. The morphology control of Au NPs on the flat substrate would be much easier to achieve if we change the curvature periodically on the flat substrate, the size of the Au NPs would be focused [45, 49]. Whereas, when referring to the substrate of 1D nanowires, because of their large curvature and the smooth surface on the atomic level due to their single-crystalline feature, the Au NPs would easily render a random growth with large particle size and broad size distributions [50, 51]. Thus, it is necessary to develop a hierarchical metal oxide substrate for the ordered growth of Au NPs to achieve superior PEC performance during the preparation of the photoelectrodes.

Herein, 3D hierarchical TiO_2 NWAs branched with TiO_2 nanoshoots and decorated with Au NPs were fabricated by the stepwise hydrothermal methods to obtain branched TiO_2 NWAs, followed by magnetron sputtering and post-annealing for the deposition of Au NPs. Magnetron sputtering technique provided an efficient route for the Au deposition, which is time-saving and easy to scale up for mass production. This designed fabrication strategy could improve the adhesion of gold NPs that were dewetted from magnetron-sputtered gold thin films through engineering 3D structures of TiO_2. The branched TiO_2 NWAs provided an ordered hierarchical platform for the formation of Au NPs during the dewetting process with uniform size, morphology, and distribution by space confinement, which was hardly achieved on a flat substrate. By combining branched TiO_2 NWAs with uniformly distributed Au NPs, the synergistic

effect between them improved the photoelectrochemical energy conversion efficiency of TiO_2 NWAs photoelectrode. 3D hierarchical-branched TiO_2 NWAs exhibited a highly efficient electron transfer pathway, and the much-enlarged surface area was beneficial for Au deposition. Au NPs could induce the amplified electromagnetic field through the SPR excitation, which could enhance the charge separation of UV-light excited TiO_2 NWAs. Besides, decoration of those Au NPs led to the effective surface passivation of those branched NWAs. Thus, the photoelectrochemical overall water splitting to effectively produce H_2 and O_2 simultaneously at the stoichiometric ratio was achieved by such Au NPs modified branched TiO_2 NWAs. It is expected to further gain insights into the novel pathways for the fabrication of Au/TiO_2 NWAs composite photoelectrode with ordered hierarchical structures and expands their applications in pure water splitting in solar energy conversion.

Experimental section

Preparation of TiO_2 NWAs

In a typical synthesis, 30 mL of deionized (DI) water was mixed with the same volume of HCl (36.0~38.0 wt%). After stirring for 5 min, 1 mL of titanium (IV) butoxide was added. Then, the mixture was stirred until the solution turned transparent. The resulting solution (7 mL) was transferred into a 25-mL Teflon-lined stainless-steel autoclave. A 1 cm×3 cm fluorine-doped tin oxide (FTO) glass was cleaned by sonication in a mixture of ethanol, acetone, and DI water for 1 h and placed into the autoclave with the conducting side facing down. The hydrothermal process was conducted at 150 °C for 15 h in an oven. The TiO_2 NWAs were washed with ethanol and DI water several times and then annealed at 550 °C for 0.5 h in air.

Preparation of branched TiO_2 NWAs

The TiO_2 NWAs were placed into a mixed solution (30 mL of DI water, 0.3 mL of $TiCl_3$, and 0.3 mL of HCl). Then, the hydrothermal process was conducted at 80 °C for 1 h in an oven. After naturally cooling, the obtained samples were rinsed with DI water and annealed at 450 °C for 0.5 h in air. The sample was denoted as S-TiO_2 (S stands for nanoshoots).

Preparation of Au NPs decorated branched TiO_2 NWAs

The Au NPs were prepared by the magnetron sputtering method on the S-TiO_2 NWAs with a current of 15 mA (E-1045 ION SPUTTER). The thickness of the deposited Au layer was adjusted by varying the sputtering time (60 s, 90 s, 120 s). Finally, the obtained samples were annealed at 300 °C for 1 h in the air via the dewetting process to obtain Au NPs. The samples were denoted as Au-x-S-TiO_2 (x stands for the sputtering time).

Characterization

The morphology and structures of the samples were investigated by scanning electron microscopy (SEM, Hitachi S-4800). Transmission electron microscopy (TEM) and high-angle annular dark field scanning transmission electron microscope (HAADF-STEM) images were obtained on a JEM-2100+microscope at 200 kV. The crystal structure of the samples was examined by an X-ray diffractometer technique (XRD, Rigaku D/Max-2400) with Cu Kα radiation ($\lambda=1.5417$ Å). The composition information of samples was explored with X-ray photoelectron spectroscopy (XPS, ESCALAB 250), with monochromatized Al Kα ($h\nu=1486.7$ eV) source and the binding energy of all the samples was calibrated by means of the C 1 s peak at 284.6 eV. The UV−visible diffuse reflection spectra (DRS) of the samples were obtained on a UV−vis spectrophotometer (Shimadzu UV-3600).

PEC measurements

The photoelectrochemical measurements were performed in a three-electrode cell on an electrochemical work station (CHI660E, Shanghai Chenhua Co. Ltd.) with the FTO-supported nanowire arrays as the working electrode, Ag/AgCl (saturated KCl) as the reference electrode, and a Pt wire as the counter electrode. The electrolyte was 0.5 M of Na_2SO_4 aqueous solution (pH=7). The PEC performance was studied under simulated solar radiation using a 500 W Xe arc lamp (100 mW/cm^2) with an AM 1.5 G filter. The

illumination intensity was calibrated to 100 mW cm^{-2} throughout the measurement. The measured potentials vs. the Ag/AgCl were converted to the reversible hydrogen electrode (RHE) scale via the Nernst equation $E_{RHE} = E_{Ag/AgCl} + 0.059 \times pH + E^0_{Ag/AgCl}$, where E_{RHE} is the converted potential vs. RHE, $E^0_{Ag/AgCl}$ is 0.209 V at 25 °C, and $E_{Ag/AgCl}$ is the experimental potential measured against Ag/AgCl reference electrode. Linear sweep voltammetry (LSV) was carried out in a potential range of −0.39 to 1.61 V (vs. RHE). The EIS spectra were measured in a frequency range of 1 Hz to 1 M Hz at 0 V (vs. Ag/AgCl). The Mott–Schottky plots were obtained at a mixed frequency of 3000 Hz in the dark. To evaluate the photo-conversion efficiency, the applied bias photon-to-current efficiency (ABPE) was measured by the following equation:

$$ABPE(\%) = ([I \times (1.23 - |V_{RHE}|) \times \eta_F]) / P_{Light} \times 100\% \tag{1}$$

where I is the photocurrent density (mA cm^{-2}), V_{RHE} is the applied bias potential (V), P_{Light} is the irradiance intensity of 100 mW cm^{-2}, and η_F is the faradaic efficiency (presumed to be 100%). The faraday efficiency (FE) was calculated by the following equation:

$$FE(\%) = (m \times n \times F) / (I \times t) \tag{2}$$

where m is the number of moles of gases (mol), n is the number of reaction electrons, F is the faraday constant (C mol^{-1}), I is the photocurrent density (mA cm^{-2}), and t is time (s). H$_2$ and O$_2$ generated from overall water splitting were conducted under identical conditions as those PEC measurements, except that a bias of 1.23 V (vs. RHE) was applied in this PEC cell. It was started by sealing the cell and purged with N$_2$ for 30 min to remove the air residue. Then, it was exposed under the simulated solar light with a fixed bias. H$_2$ and O$_2$ produced were collected into a syringe and analyzed on the gas chromatograph (Shimadzu, GC-2014, Japan) periodically, which was equipped with a thermal conductivity detector (TCD).

Results and discussion

Morphology and crystal structure of Au–S-TiO$_2$ NWAs

The schematic diagram of the synthesis process of Au–S-TiO$_2$ NWAs is shown in Fig. 1. The TiO$_2$ and S-TiO$_2$ NWAs were synthesized by a consequential hydrothermal method on FTO glasses [37]. Then, Au was deposited onto the as-prepared NWAs samples via magnetron sputtering and post-annealing, which is a physical method for the growth of Au NPs, with the advantage of readily scale-up for mass production. Furthermore, the SEM images of the obtained
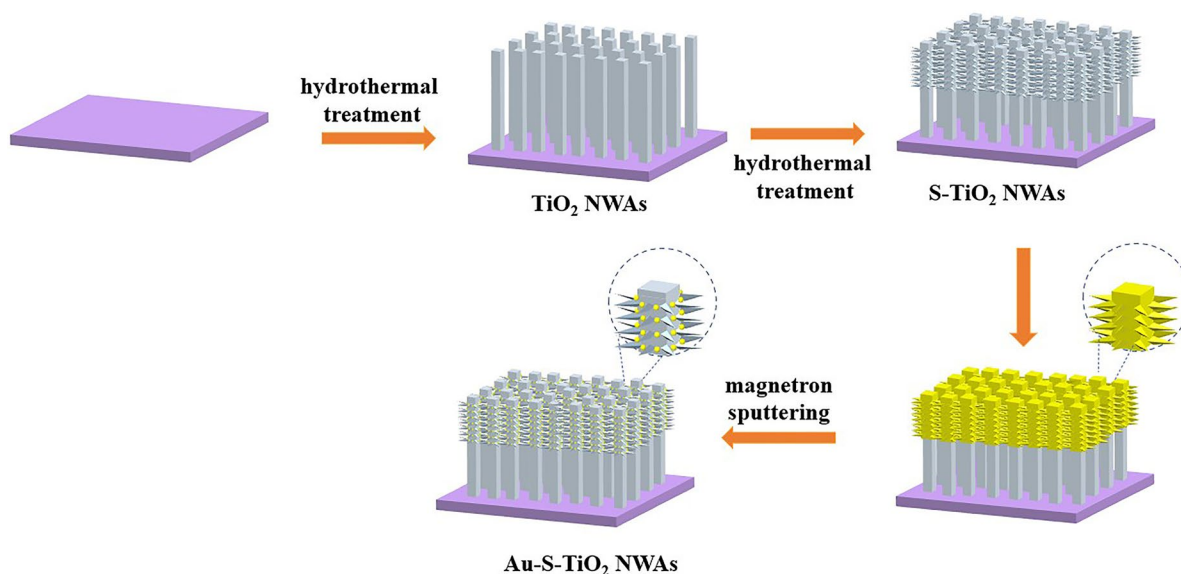

Fig. 1 Schematic diagram of the synthesis process of Au–S-TiO$_2$ NWAs

samples are displayed in Fig. 2a–e. Figure 2a shows the TiO$_2$ NWAs vertically grew on the FTO substrate with a smooth surface. After going through the secondary hydrothermal growth process, the surface of the S-TiO$_2$ NWAs became rough. As shown in Fig. 2b, each TiO$_2$ nanowire is covered with short branches that looked like emerging shoots, which can significantly enlarge the specific surface area of TiO$_2$ NWAs. The SEM image of S-TiO$_2$ NWAs after sputtering of Au is shown in Figure S1. A thin layer of Au film was uniformly coated on both the nanowire arrays and the newly grown nanoshoots. In Fig. 2c–e, Au particles are deposited on S-TiO$_2$ samples after the annealing for the dewetting process. The amount of Au deposited can be controlled by sputtering time. When the sputtering time was prolonged to 120 s, the S-TiO$_2$ NWAs were fully covered by Au particles, which would further drastically increase the surface roughness of the branched NWAs (Fig. 2e). The content of Au obtained from Au-60-S-TiO$_2$, Au-90-S-TiO$_2$, and Au-120-S-TiO$_2$ NWAs through EDX spectra are presented in Table S1. It showed that with increasing sputtering time, the content of Au increased. Besides, the color of the substrate changed from gray to pink-purple owing to the SPR effect of Au particles (Fig. 2f).

The morphology of the Au–S-TiO$_2$ NWAs was further examined by TEM (Figs. 3 and S2). As shown in Figs. 3a and 3b, the image of Au-90-S-TiO$_2$ NWAs manifested that the as-prepared sample consisted of the S-TiO$_2$ nanowires and Au particles. A 3D nanostructure with nanoshoots was grown on the backbones of the TiO$_2$ NWAs. In addition, Au particles were successfully loaded on the S-TiO$_2$ nanowires with narrow size distributions (Fig. 3a inset). HRTEM image revealed a good lattice match of the samples (Figs. 3c and 3d). The lattice fringe spacings of 0.31 and 0.25 nm were ascribed to the (110) and (101) crystalline planes of rutile TiO$_2$ [41]. Furthermore, the lattice spacing of Au particles was measured to be 0.23 and 0.20 nm, which could be attributed to the Au (111) and (200) planes [39]. It is suggested that the nanowire backbones and shoots of Au-90-S-TiO$_2$ were in the rutile phase, and Au nanoparticles were decorated on the outer surface of S-TiO$_2$ between the gaps of those shoots. It was worth noting that all the Au NPs deposited on this branched hierarchical structure presented a narrowed size distribution, which is quite different from their analogs on the flat substrate, as shown in Figure S3. In that case, in the absence of the space confinement of the complex substrate, the Au NPs rendered a broad size distribution, different shapes, and random location on the nanowires. In our work, during the annealing of Au films sputtered on the S-TiO$_2$ sample, the dewetting process of deposited Au would occur. In order
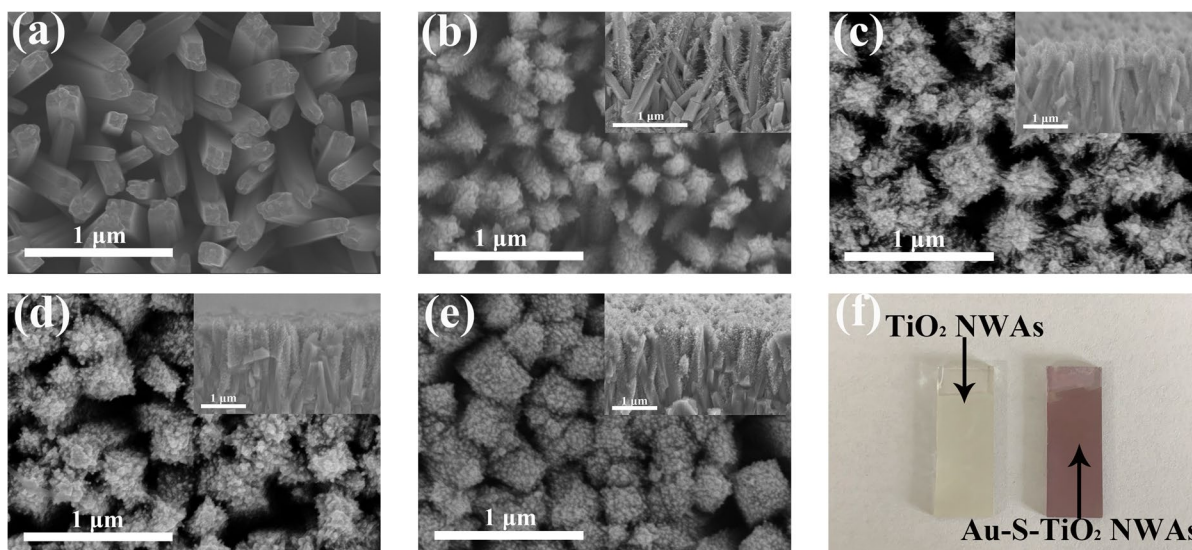
Fig. 2 SEM images of **a** TiO$_2$, **b** S-TiO$_2$, **c** Au-60-S-TiO$_2$, **d** Au-90-S-TiO$_2$, **e** Au-120-S-TiO$_2$ NWAs, and **f** the digital photographs of the samples
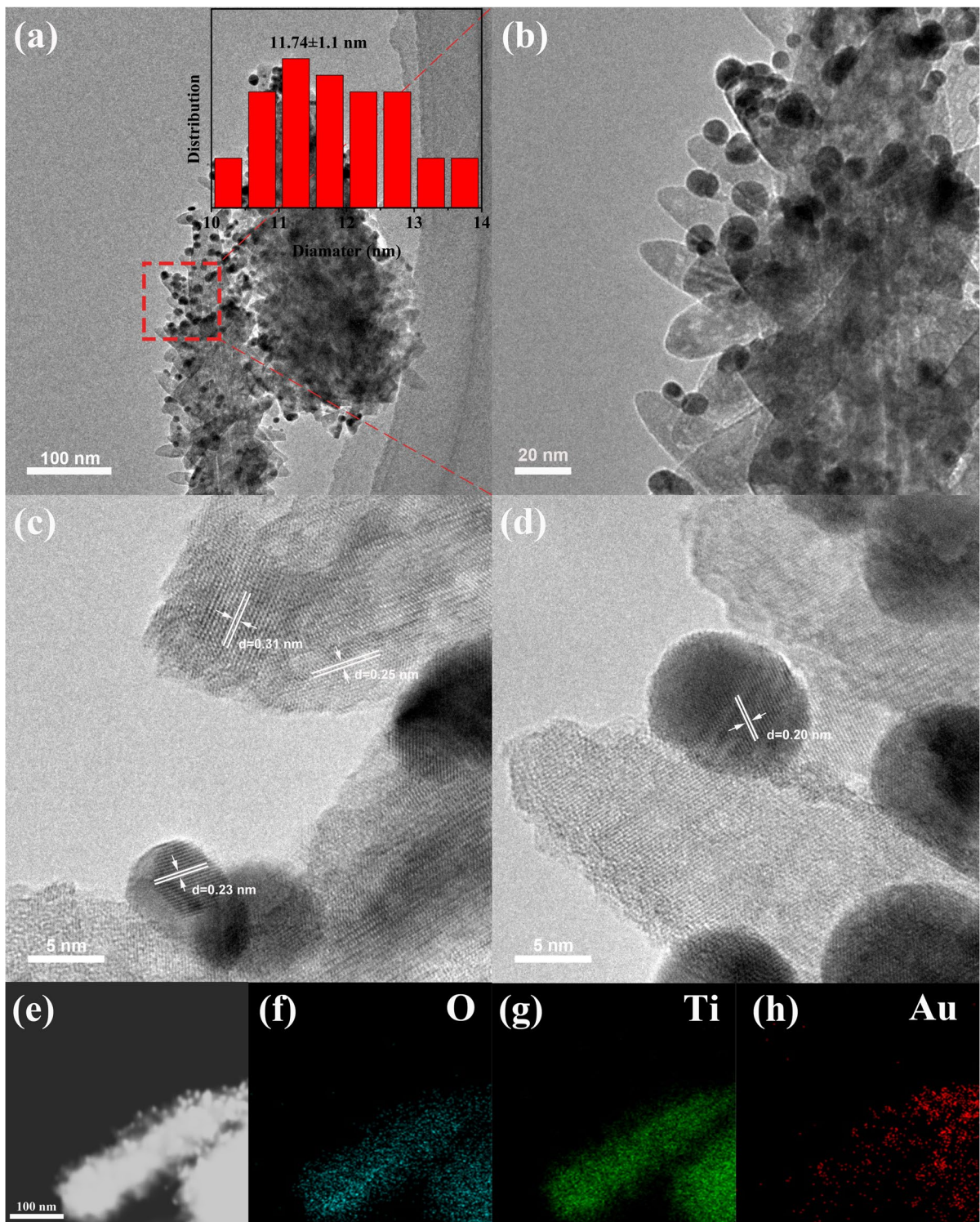
Fig. 3 **a**, **b** TEM images, **c**, **d** HRTEM images, **e** HAADF-STEM image of Au-90-S-TiO$_2$ NWAs; EDS mappings of **f** Ti, **g** O, and **h** Au of Au-90-S-TiO$_2$ NWAs

to minimize their surface energy, the Au NPs were prone to migrate to the bottom of the gaps induced by those TiO_2 nanoshoots to form multiple interfaces with neighboring nanoshoots from different directions. The space between the adjacent nanoshoots was acting as the template for the space confinement of the growth for the Au NPs. As a result, they exhibited an intensive size distribution and a uniform morphology (spherical particles), which would be beneficial from the light trapping at defined wavelengths by the SPR effect. Besides, the TEM images in Figure S2e–g show that with increasing sputtering time, the diameter of gold particles gradually increased (Table S1). The atomic ratio of Au in these samples increased linearly, which indicated this physical deposition process was highly controllable. The element-mapping images in Fig. 3f–h further confirm the existence of the elements Ti, O, and Au with uniform distribution all over the nanowire.

The crystallinity and phase composition of the as-synthesized samples were characterized by XRD (Figure S4). All the peaks can be attributed to the tetragonal TiO_2 of the rutile phase (JCPDS 21–1276). Compared to the XRD patterns of pristine TiO_2 NWAs, no additional diffraction peaks of the S-TiO_2 NWAs were observed, indicating the shoots of Au–S-TiO_2 samples were also in rutile phase. The absence of the typical diffraction peaks of Au is mainly because its content was below the detection limit of the XRD device.

Optical properties and surface chemical states of Au-S-TiO_2 NWAs

The optical properties of TiO_2, S-TiO_2, and Au–S-TiO_2 NWAs were obtained by DRS spectra (Fig. 4a). Compared with pristine TiO_2 NWAs, the absorption edge for the other four samples was slightly red-shifted. The decorating of Au particles can further enhance the visible light response relatively to S-TiO_2 NWAs, contributed from the SPR effect of Au particles. The intensity of the absorption peak due to the SPR effect (~520 nm) was gradually pronounced along with the increased amount of Au by sputtering. It is worth noting that those Au NPs with uniform morphology in size and shape rendered a much more intensive SPR peak than that of their counterparts with very broad size distributions. The curves based on the Kubelka–Munk function versus the energy of light are shown in Fig. 4b. The band gaps of TiO_2 NWAs, S-TiO_2 NWAs, Au-60-S-TiO_2 NWAs, Au-90-S-TiO_2 NWAs, and Au-120-S-TiO_2 NWAs were 3.1, 2.99, 2.96, 2.94, 2.92 eV, respectively. Decorating Au particles could slightly narrow down the band gap of S-TiO_2 samples, and such tuning of band edges could also enhance the visible light absorption in addition to the SPR effect of Au nanoparticles.

Furthermore, the surface compositions and chemical states of TiO_2, S-TiO_2, and Au-90-S-TiO_2 NWAs were analyzed by XPS. The full survey spectra of the Au-90-S-TiO_2 NWAs displayed the presence of
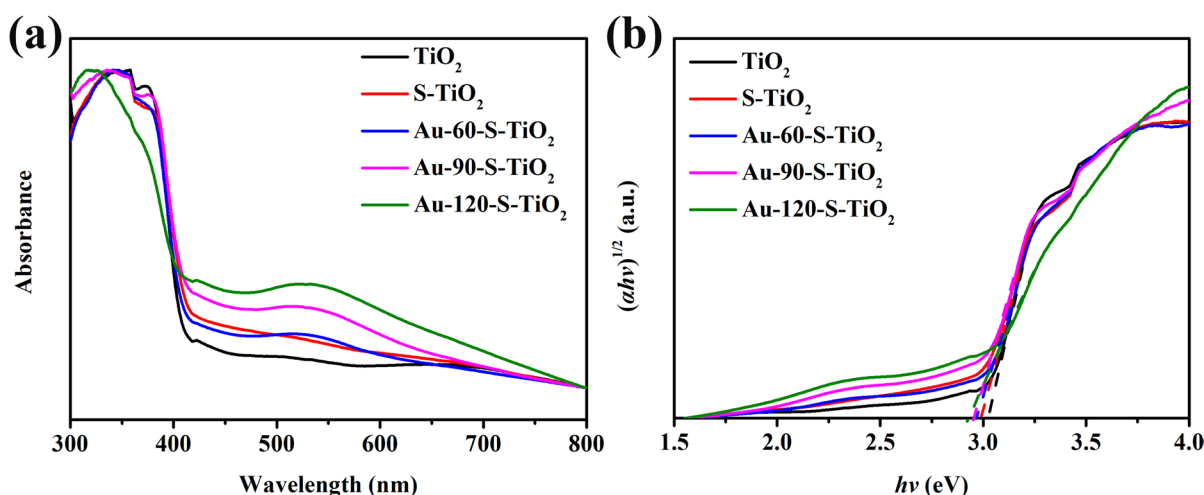
Fig. 4 **a** UV–vis diffuse reflectance spectra (DRS) and **b** corresponding band gaps estimated by K-M function for various TiO_2 NWA samples
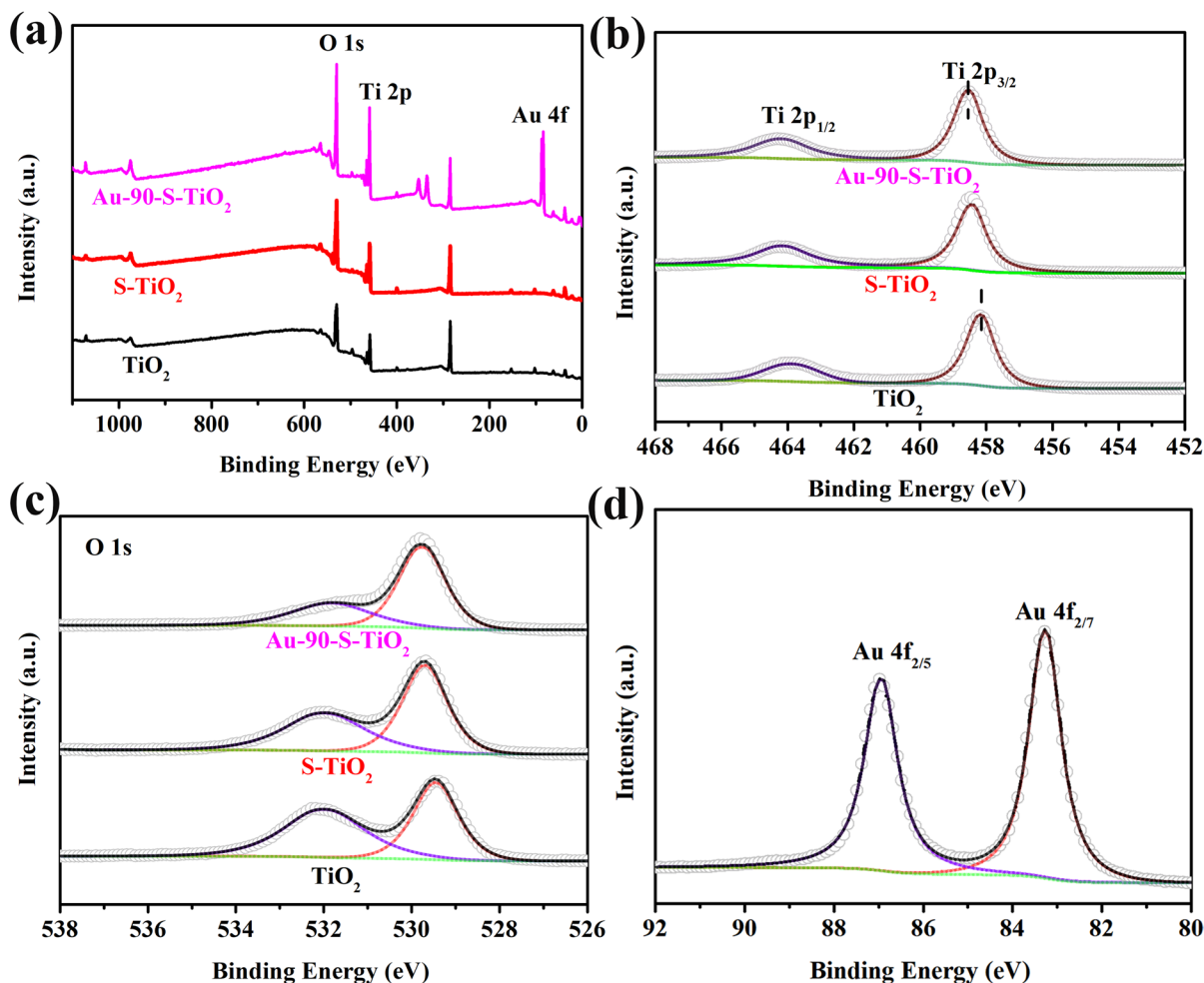
Fig. 5 **a** XPS survey spectra of TiO_2, S-TiO_2, and Au-90-S-TiO_2 NWAs. High-resolution XPS spectra of **b** Ti 2p, **c** O 1 s for TiO_2, S-TiO_2, and Au-90-S-TiO_2 NWAs. **d** Au 4f XPS spectrum of Au-90-S-TiO_2 NWAs

Ti, O, and Au (Fig. 5a). Figure 5b shows the Ti 2p XPS spectra for those three samples. Au-90-S-TiO_2 exhibited two peaks at 458.5 and 464.1 eV, which could be assigned to Ti $2p_{3/2}$ and Ti $2p_{1/2}$ of Ti^{4+} in TiO_2, respectively. There was a small shift of 0.4 eV for the Ti $2p_{3/2}$ peaks from 458.1 of pristine TiO_2 to 458.5 eV of Au-90-S-TiO_2, implying the electron transfer between Au particles and TiO_2 NWAs. The high-resolution O 1 s XPS spectra had two peaks centered at 529.3 and 531.6 eV (Fig. 5c). The peak located at 529.3 eV could be assigned to O^{2-} in the TiO_2 lattice. The binding energy of O 1 s at 531.6 eV was attributed to Ti–OH [1]. The Au 4f XPS spectrum was ascribed to Au $4f_{7/2}$ and Au $4f_{5/2}$ located

at binding energies of 83.3 and 86.9 eV, which confirmed the metallic Au in Au-90-S-TiO_2 (Fig. 5d) [39, 40].

Evaluation of PEC overall water splitting performances

The LSV curves for the prepared samples are shown in Fig. 6a. After the growth of branches, the S-TiO_2 NWAs displayed a pronounced photocurrent of 1.28 mA cm^{-2} at 1.23 V vs. RHE, higher than that of the pristine TiO_2 (0.73 mA cm^{-2}). It hinted that the light absorption in S-TiO_2 NWAs was greatly improved due to their branched nanostructure for
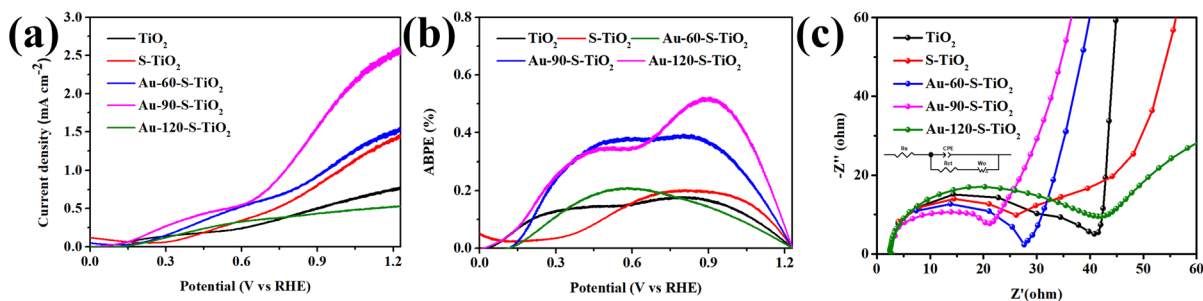
Fig. 6 **a** LSV curves measured at 1.23 V vs. RHE, **b** applied bias photo-to-current efficiency (ABPE) curves, **c** EIS curves of TiO$_2$, S-TiO$_2$, and various Au NP-modified S-TiO$_2$ NWAs

effective light multiple reflection and trapping, which was beneficial for the enhanced charge separations. The photocurrent of the obtained samples was further improved after decoration with Au particles. By prolonging the sputtering time (60, 90, and 120 s), different photocurrent density–voltage (*j*–V) curves can be obtained. The Au-90-S-TiO$_2$ NWAs achieved the highest photocurrent density of 2.56 mA cm^{-2} at 1.23 V vs. RHE, which was over three times higher than that of the pristine TiO$_2$. However, the current density declined when the sputtering time extended to 120 s. This decay occurred because overloading excessive Au NPs with large size would block the light absorption of TiO$_2$ NWAs, then restricting the generation of UV-excited charge carriers. In addition, the interfacial surface area between the TiO$_2$ nanowires of the composite electrode and the electrolyte was also reduced, restricting the transfer of photogenerated holes to the electrolyte for water oxidation. Thus, the sample of Au-90-S-TiO$_2$ was selected for further investigation in the following study.

The applied bias photon-to-current efficiency (ABPE) spectra of the prepared photoelectrodes are displayed in Fig. 6b. The Au-90-S-TiO$_2$ NWAs displayed the largest efficiency of 0.554% at 0.87 V vs. RHE, which was 2.73 and 3.08 times higher than those of S-TiO$_2$ (0.203% at 0.80 V vs. RHE), and TiO$_2$ (0.180% at 0.80 V vs. RHE). The improved ABPE of Au-90-S-TiO$_2$ NWAs suggested the much enhanced photoelectric conversion efficiency by the Au-TiO$_2$ composite photoelectrodes.

To further study the charge transfer process of the photoelectrodes, EIS was measured in the dark. As shown in Fig. 6c, the radii of the semicircle of the Au-90-S-TiO$_2$ NWAs was the smallest. It also means that the Au-90-S-TiO$_2$ NWAs exhibited the

lowest electron-transfer resistance and fastest charge transfer kinetics, which contributed to the remarkable enhanced PEC performance. Besides, their EIS plots under simulated solar light illumination were also recorded (Figure S5). All the radius of the plots for various electrodes followed the same order as they were measured in dark, indicating Au-90-S-TiO$_2$ NWAs also exhibited the optimal charge transfer efficiency. It was worth noting that the charge transfer resistance of all the samples was reduced upon the light illumination.

Mott–Schottky measurements of the samples were performed to investigate the charge transport behavior. All photoelectrodes showed positive slopes, which implied that TiO$_2$, S-TiO$_2$, and Au-90-S-TiO$_2$ NWAs are n-type semiconductors (Figure S6a–c). Compared to pristine TiO$_2$, the flat band potential for S-TiO$_2$ and Au-90-S-TiO$_2$ showed a slight positive shift. In addition, the carrier density can be calculated according to the following equation:

$$N_d = [2/(q\varepsilon\varepsilon_0)][d(1/c^2)/dV]^{-1} \qquad (3)$$

where N_d is the carrier density, electronic charge $q = 1.6 \times 10^{-19}$ C, dielectric constant of TiO$_2$ $\varepsilon = 86$ F cm^{-1}, permittivity of vacuum $\varepsilon_0 = 8.85 \times 10^{-14}$ F cm^{-1}. The calculated carrier density were 5.2×10^{21}, 1.64×10^{22}, and 8.97×10^{22} cm^{-3} for TiO$_2$, S-TiO$_2$, and Au-90-S-TiO$_2$ NWAs. It was worth noting that the carrier density of the Au-90-S-TiO$_2$ NWAs was 17.2 times higher than that of the pristine TiO$_2$ sample, which was attributed to the branched nanowire structure and the decoration of Au nanoparticles.

To further illustrate the improvement of PEC performance, the light absorption efficiency (LHE), charge separation efficiency (η_{sep}), and injection

efficiency (η_{inj}) of those three electrodes were studied. Theoretically, J_{PEC} is governed by the relation

$$J_{PEC} = J_{abs} \times \eta_{sep} \times \eta_{inj} \qquad (4)$$

where J_{abc} is the photocurrent density at 100% internal quantum efficiency, η_{sep} is the photogenerated electron−hole separation efficiency for producing surface-reaching holes, and η_{inj} is the efficiency of surface-reaching holes participating in desired electrochemical reactions[40]. The value of J_{abs} was calculated by multiplying the LHE of each wavelength throughout each step of the integration (Figs. 7a, 7b, and S7) [27, 52, 53]. The J_{abs} values of TiO_2, $S-TiO_2$, and $Au-90-S-TiO_2$ NWAs were calculated to be 5.1, 6.6, and 8.3 mA cm^{-2}, respectively (Fig. 7b). The charge separation and injection

efficiencies were determined by adding a fast hole scavenger to the electrolyte. Since Na_2SO_3 possesses greatly fast oxidation kinetics, which is suitable as a hole scavenger. The photocurrent density of sulfite oxidation ($J_{Na_2SO_3}$) is shown in Figure S8. The η_{sep} of the samples can be determined by the equation of $\eta_{sep} = J_{Na_2SO_3}/J_{abs}$. For the sample of Au-90-S-TiO$_2$ NWAs, the charge separation efficiency was calculated to be 36.77% at 1.23 V vs. RHE (Fig. 7c), much larger than that of pristine TiO_2 (13.97%) and S-TiO$_2$ NWAs (27.62%). The reason for this phenomenon was that the decoration of Au particles can inhibit electron/hole recombination. On the basis of the measured photocurrent density, η_{inj} was calculated through the relationship $\eta_{inj} = J_{PEC}/J_{Na_2SO_3}$. In Fig. 7d, the η_{inj} value of Au-90-S-TiO$_2$ NWAs has achieved 83.93%, which was the highest value of all
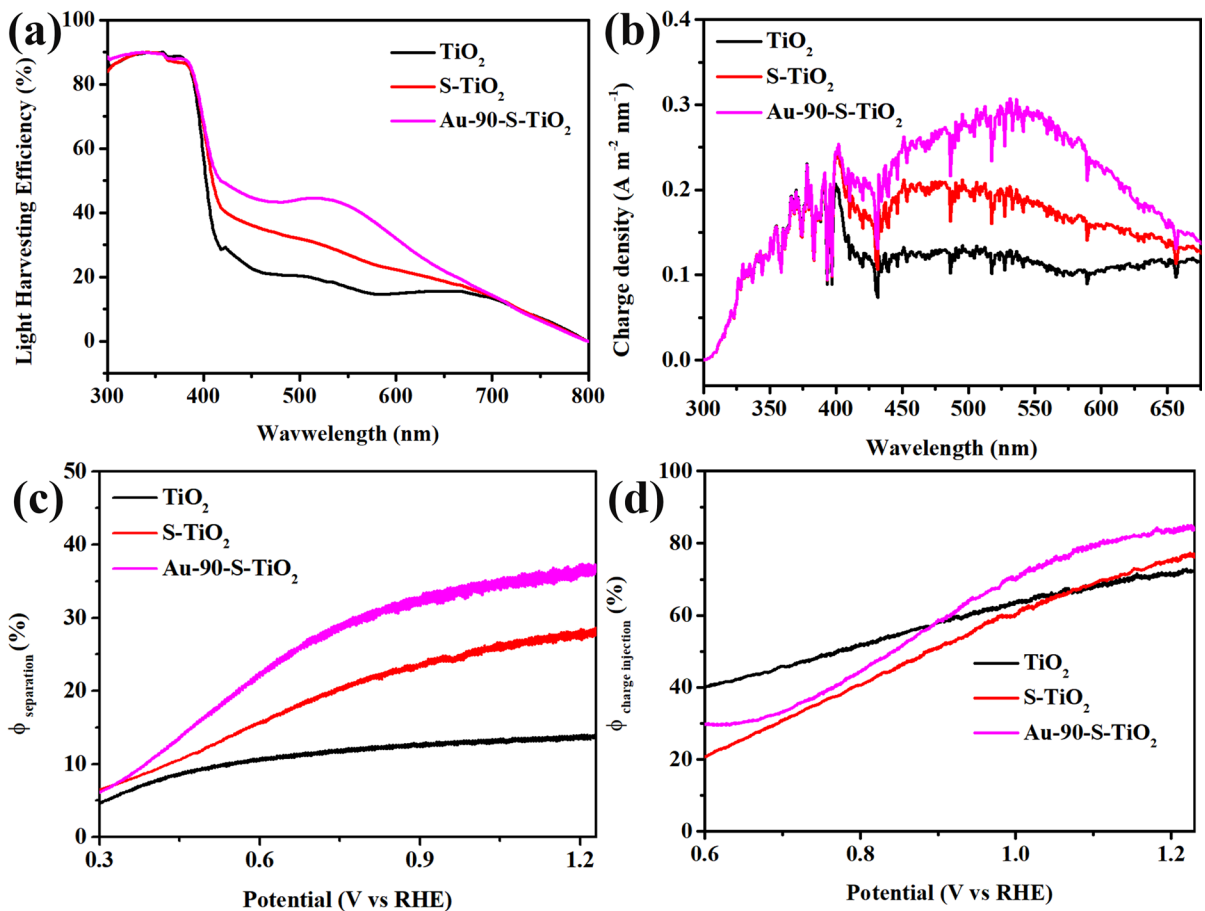

Fig. 7 **a** The LHE plots, **b** the charge density (the J_{abs} is the integration of charge density by wavelength), **c** charge separation efficiency ηsep$_{sep}$, and **d** charge-injection efficiency η_{inj} of TiO$_2$, S-TiO$_2$, and Au-90-S-TiO$_2$ NWAs.

the photoelectrodes. The increased η_{inj} in Au-90-S-TiO$_2$ NWAs was attributed to the synergetic effect between Au NPs and branched TiO$_2$ NWAs for the improvement of the charge injection efficiency at the interface between the composite electrode and the electrolyte. Furthermore, the enhancement of the injection efficiency indicated that it was highly efficient toward water oxidation.

The anodic photocurrent dynamics of photoelectrodes was measured to further explore the charge recombination behavior, by which their apparent charge carrier lifetime could be determined (Fig. 8a) [10, 54].The transient time constant (τ, the specific calculations are in Figure S9) were 11.2 s, 4.8 s, and 2.6 s for TiO$_2$, S-TiO$_2$, and Au-90-S-TiO$_2$ NWAs

(Fig. 8b). The Au-90-S-TiO$_2$ NWAs had good injection efficiency and separation efficiency, leading to rapid separation of photogenerated electron–hole pairs, which were quickly injected into the electrolyte through the electrode/electrolyte interface. So, the lifetime of the photogenerated charge carriers of the Au-90-S-TiO$_2$ NWAs was the shortest.

In a typical three-electrode cell, the reactivity of the photoelectrodes was measured for PEC overall water splitting under simulated solar light. The amounts of H$_2$ and O$_2$ were analyzed by GC equipped with a thermal conductivity detector. The histogram showed that hydrogen and oxygen evolved at a stoichiometric ratio of approximately 2:1 at the end of the reaction. In Fig. 9a, the highest amount of H$_2$
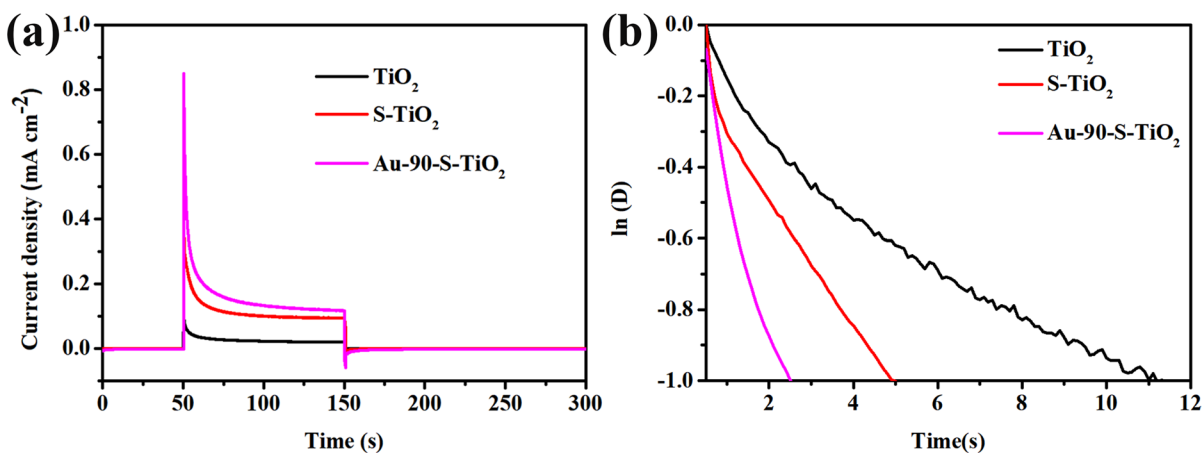
Fig. 8 a Chronoamperometry curves of TiO$_2$, S-TiO$_2$, Au-90-S-TiO$_2$ NWAs at 0.6 V vs. RHE. **b** ln(D)-t plots for TiO$_2$, S-TiO$_2$, and Au-90-S-TiO$_2$ NWAs
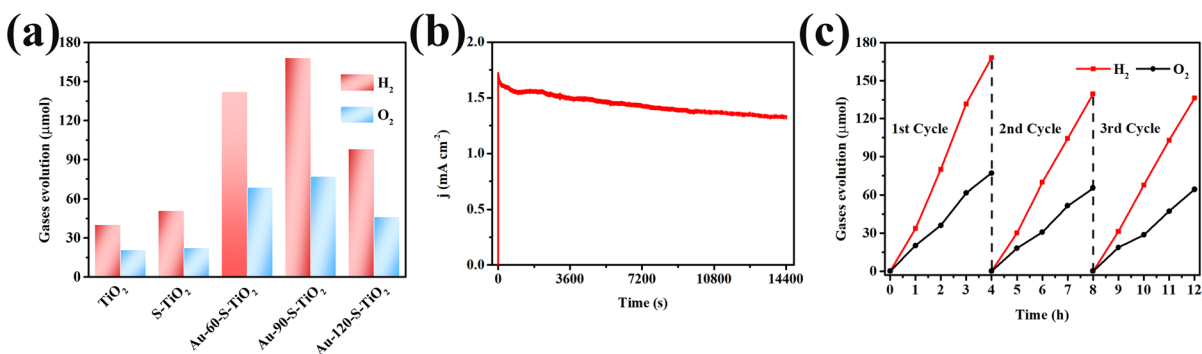

Fig. 9 a The amounts of H$_2$ and O$_2$ produced by TiO$_2$, S-TiO$_2$, and Au-90-S-TiO$_2$ NWAs at the fourth hour. **b** The photocurrent curve of the Au-90-S-TiO$_2$ NWAs measured at 1.23 V vs. RHE. **c** Recycling test of the evolution of H$_2$ and O$_2$ for Au-90-S-TiO$_2$ NWAs

(168 μmol) and O_2 (77 μmol) were generated by Au-90-S-TiO_2 when the reaction lasted for 4 h, which was 4 times higher than that of the pristine TiO_2 sample. In addition, the FE for the production of generated gases reached 87.9%. The photocurrent curve of the Au-90-S-TiO_2 NWAs showed a negligible drop within 4 h, which demonstrated the high stability in PEC water splitting reaction (Fig. 9b). In addition, the stability of the electrode was examined by a recycling experiment of the Au-90-S-TiO_2 carried out at 1.23 V vs RHE under simulated sunlight for 4 h at each cycle. It can be seen that the ratio of H_2 to O_2 was close to 2:1 within three cycles. The yield of H_2 and O_2 in the second and third cycles was similar, only a 16.7% decline from the initial one, suggesting the favorable stability of the electrode under long-term operation. The SEM image and XRD patterns of the Au-90-S-TiO_2 sample after 3 cycles of reaction is present in Figure S10. The leakage of Au may occur during the PEC reactions, and this could explain the slight decline of reactivity for Au-90-S-TiO_2 in the recycling test.

A possible charge transfer mechanism of Au-90-S-TiO_2 NWAs (Fig. 10) was proposed on the basis of the above results and analysis. Under the simulated solar light irradiation, both branched TiO_2 NWAs and Au were photoexcited. The TiO_2 nanowires with shoots can scatter the incident light and extend the light transport path, improving the utilization of the light, by means of this, the electrons of TiO_2 were photoexcited from the valence band (VB) to the conduction band (CB). Au nanoparticles acted as the photosensitizers, enhancing the light absorption and amplifying the electromagnetic field through the SPR excitation [41]. The uniform size and distribution of Au NPs led to the improved light absorption in a narrow band region by the SPR effect (~520 nm). Because of the limited loading amount of Au NPs, and the simultaneous excitation of branched TiO_2 NWAs and Au NPs, it is reasonable to deduce that the improvement of the reactivity for water splitting was mainly due to the near-field electromagnetic mechanism (NFEM) and surface passivation of TiO_2 nanowires. The amplified electromagnetic field through the SPR excitation of Au NPs can increase the light-trapping ability and promote the generation and separation of electron–hole pairs in the branched TiO_2 NWAs [51, 55]. The space confinement and localization of Au NPs by branched TiO_2 NWAs vastly increased the interfacial area between those two components with the intimate contact, which could greatly boost the possible charge transfer [56]. In addition, maximized surface passivation of branched TiO_2 NWAs by uniform distributed Au NPs could significantly reduce the loss of photogenerated holes via electron–hole recombination at the surface trap states. As a result, The electrons produced by these two components could transfer to the FTO glass rapidly due to intimate contact between NWAs core and FTO glass, and then through the external circuit
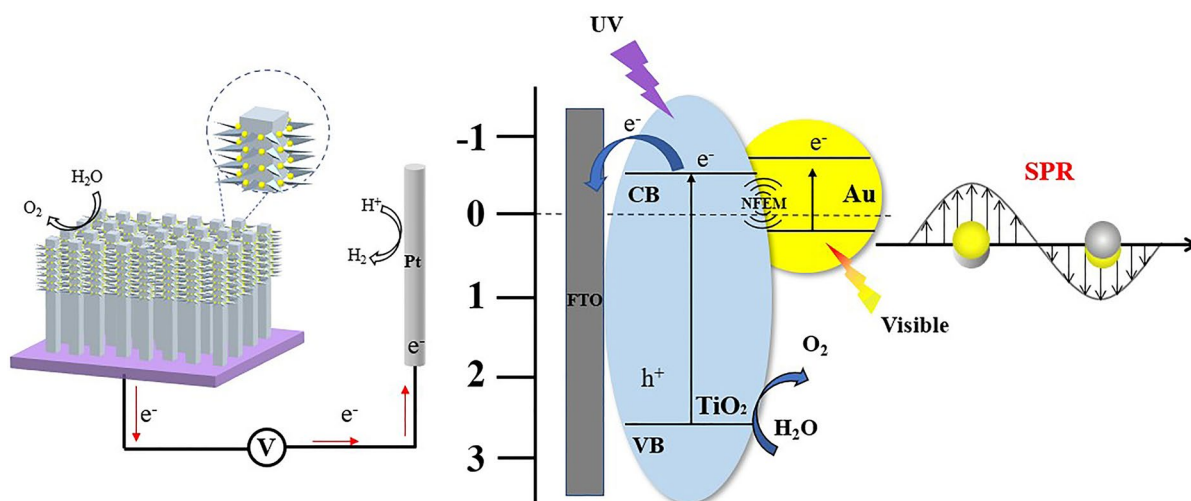
Fig. 10 The proposed mechanism for PEC water splitting by Au-90-S-TiO_2 NWAs

to the Pt electrode where eventually, protons were reduced to hydrogen by the electrons. In the meantime, holes left on the VB of TiO_2 could transfer to the surface of the electrode and finally oxidize water to oxygen at the outer surface of the TiO_2 nanoshoots on the photoanode. The appropriate sputtering time of Au (90 s) on S-TiO_2 NWAs optimized the light penetration and utilization and provide sufficient active sites for the water redox reactions. All these factors combined resulted in much enhancement of the PEC overall water splitting efficiency.

Conclusion

In summary, 3D hierarchical Au–S-TiO_2 NWAs was fabricated via a stepwised hydrothermal route combined with the magnetron sputtering and post-annealing for the deposition of Au NPs. The TiO_2 nanowires with shoots helped for the scattering of the incident light and extend the light transport path, improving the utilization of the light. The magnetron sputtering and post-dewetting process of Au provides a much more reliable technique for the mass production of uniformly distributed metal NPs on a complicated rough surface of the electrode substrate. The space confinement originated by S-TiO_2 NWAs led to the great improvement of the quality of deposited Au NPs, both in size and their distribution. The designed fabrication strategy improved the adhesion of gold NPs that were dewetted from magnetron sputtered gold thin films through engineering the 3D structure of TiO_2. The Au–S-TiO_2 NWAs electrode exhibited dramatically enhanced reactivity for the PEC overall water splitting for the production of H_2 and O_2, and the FE could reach 87.9%. The improved light absorption by branched TiO_2 NWAs, the NFEM of Au NPs, and the surface passivation of TiO_2 NWAs by Au NPs together showed the synergistic effect of such reinforcement. This work provides a potential strategy for the deposition of regulated Au NPs on a predesigned ordered hierarchical substrate (in this case, branched TiO_2 NWAs) for the improvement of the performance of the PEC device. It is anticipated that our work would reveal some insights into the fabrication of highly efficient metal/semiconductor nanocomposite electrodes and expand their potential applications in overall water splitting by solar energy conversion.

Declarations

Conflict of interest The authors declare no competing interests.

References

1. Bashiri R, Samsudin MFR, Mohamed NM, Suhaimi NA, Ling LY, Sufian S, Kait CF (2020) Influence of growth time on photoelectrical characteristics and photocatalytic hydrogen production of decorated Fe_2O_3 on TiO_2 nanorod in photoelectrochemical cell. Appl Surf Sci 510:145482. https://doi.org/10.1016/j.apsusc.2020.145482

2. Deng J, Su Y, Liu D, Yang P, Liu B, Liu C (2019) Nanowire photoelectrochemistry. Chem Rev 119(15):9221–9259. https://doi.org/10.1021/acs.chemrev.9b00232

3. Dey S, Roy SC (2021) Hydrothermal temperature-controlled size and distribution of CeO_2 nanoparticles over TiO_2 nanorods: heterojunction characteristics and photoelectrochemical performance. Ceram Int 47(10):14603–14611. https://doi.org/10.1016/j.ceramint.2021.02.043

4. Han Y, Wu J, Li Y, Gu X, He T, Zhao Y, Huang H, Liu Y, Kang Z (2022) Carbon dots enhance the interface electron transfer and photoelectrochemical kinetics in TiO_2 photoanode. Appl Catal B 304:120983. https://doi.org/10.1016/j.apcatb.2021.120983

5. Ma H, Yuan C, Wang X, Wang H, Long Y, Chen Y, Wang Q, Cong Y, Zhang Y (2021) Deposition of CeO_2 on TiO_2 nanorods electrode by dielectric barrier discharge plasma to enhance the photoelectrochemical performance in high chloride salt system. Sep Purif Technol 276:119252. https://doi.org/10.1016/j.seppur.2021.119252

6. Ning FY, Shao MF, Xu SM, Fu Y, Zhang RK, Wei M, Evans DG, Duan X (2016) TiO_2/graphene/NiFe-layered double hydroxide nanorod array photoanodes for efficient photoelectrochemical water splitting. Energy Environ Sci 9(8):2633–2643. https://doi.org/10.1039/c6ee01092j

7. Rao PM, Cai L, Liu C, Cho IS, Lee CH, Weisse JM, Yang P, Zheng X (2014) Simultaneously efficient light absorption and charge separation in WO_3/$BiVO_4$ core/shell nanowire photoanode for photoelectrochemical water oxidation. Nano Lett 14(2):1099–1106. https://doi.org/10.1021/nl500022z

8. Shi X, Choi IY, Zhang K, Kwon J, Kim DY, Lee JK, Oh SH, Kim JK, Park JH (2014) Efficient photoelectrochemical hydrogen production from bismuth vanadate-decorated tungsten trioxide helix nanostructures. Nat Commun 5:4775–4782. https://doi.org/10.1038/ncomms5775

9. Su JY, Geng P, Li XY, Chen GH (2016) Graphene-linked graphitic carbon nitride/TiO_2 nanowire arrays heterojunction for efficient solar-driven water splitting. J Appl Electrochem 46(8):807–817. https://doi.org/10.1007/s10800-016-0928-2

10. Yang H, Bright J, Kasani S, Zheng P, Musho T, Chen B, Huang L, Wu N (2018) Metal-organic framework coated titanium dioxide nanorod array p-n heterojunction photoanode for solar water-splitting. Nano Res 12(3):643–650. https://doi.org/10.1007/s12274-019-2272-4

11. Zhang RK, Shao MF, Xu SM, Ning FY, Zhou L, Wei M (2017) Photo-assisted synthesis of zinc-iron layered double hydroxides/TiO_2 nanoarrays toward highly-efficient photoelectrochemical water splitting. Nano Energy 33:21–28. https://doi.org/10.1016/j.nanoen.2017.01.020

12. Zhang X, Liu Y, Lee ST, Yang SH, Kang ZH (2014) Coupling surface plasmon resonance of gold nanoparticles with slow-photon-effect of TiO_2 photonic crystals for synergistically enhanced photoelectrochemical water splitting. Energy Environ Sci 7(4):1409–1419. https://doi.org/10.1039/c3ee43278e

13. Huang KL, Li CH, Zhang XL, Meng XC, Wang L, Wang WT, Li ZZ (2020) TiO_2 nanorod arrays decorated by nitrogen-doped carbon and g-C_3N_4 with enhanced photoelectrocatalytic activity. Appl Surf Sci 518:146219. https://doi.org/10.1016/j.apsusc.2020.146219

14. Li YG, Wang RR, Li HJ, Wei XL, Feng J, Liu KQ, Dang YQ, Zhou AN (2015) Efficient and stable photoelectrochemical seawater splitting with TiO_2@g-C_3N_4 nanorod arrays decorated by Co-Pi. J Phys Chem C 119(35):20283–20292. https://doi.org/10.1021/acs.jpcc.5b05427

15. Pang Y, Zang W, Kou Z, Zhang L, Xu G, Lv J, Gao X, Pan Z, Wang J, Wu Y (2020) Assembling of Bi atoms on TiO_2 nanorods boosts photoelectrochemical water splitting of semiconductors. Nanoscale 12(7):4302–4308. https://doi.org/10.1039/d0nr00004c

16. Wang LL, Tang GG, Liu S, Dong HL, Liu QQ, Sun JF, Tang H (2022) Interfacial active-site-rich 0D Co_3O_4/1D TiO_2 p-n heterojunction for enhanced photocatalytic hydrogen evolution. Chem Eng J 428:131338. https://doi.org/10.1016/j.cej.2021.131338

17. Liu Z, Xu K, Yu H, Zhang M, Sun Z (2021) In-situ preparation of double Z-scheme Bi_2S_3/$BiVO_4$/TiO_2 ternary photocatalysts for enhanced photoelectrochemical and photocatalytic performance. Appl Surf Sci 545:148986. https://doi.org/10.1016/j.apsusc.2021.148986

18. Yu H, Zhang M, Wang YF, Lv JG, Liu YM, He G, Sun ZQ (2021) Low-temperature strategy for vapor phase hydrothermal synthesis of C\N\S-doped TiO_2 nanorod arrays with enhanced photoelectrochemical and photocatalytic activity. J Ind Eng Chem 98:130–139. https://doi.org/10.1016/j.jiec.2021.03.021

19. Zhang SC, Liu ZF, Yan WG, Guo ZG, Ruan MN (2020) Decorating non-noble metal plasmonic Al on a TiO_2/Cu_2O photoanode to boost performance in photoelectrochemical water splitting. Chin J Catal 41(12):1884–1893. https://doi.org/10.1016/S1872-2067(20)63637-3

20. Hoang S, Guo S, Hahn NT, Bard AJ, Mullins CB (2012) Visible light driven photoelectrochemical water oxidation on nitrogen-modified TiO_2 nanowires. Nano Lett 12(1):26–32. https://doi.org/10.1021/nl2028188

21. Wang G, Wang H, Ling Y, Tang Y, Yang X, Fitzmorris RC, Wang C, Zhang JZ, Li Y (2011) Hydrogen-treated TiO_2 nanowire arrays for photoelectrochemical water splitting. Nano Lett 11(7):3026–3033. https://doi.org/10.1021/nl201766h

22. Xiong XX, Li C, Yang XY, Shu Y, Jin DQ, Zang Y, Shu YS, Xu Q, Hu XY (2020) In situ grown TiO_2 nanorod arrays functionalized by molecularly imprinted polymers for salicylic acid recognition and detection. J Electroanal Chem 873:114394. https://doi.org/10.1016/j.jelechem.2020.114394

23. Zhang SC, Liu ZF, Chen D, Guo ZG, Ruan MN (2020) Oxygen vacancies engineering in TiO_2 homojunction/ZnFe-LDH for enhanced photoelectrochemical water oxidation. Chem Eng J 395:125101. https://doi.org/10.1016/j.cej.2020.125101

24. Li YY, Wang JG, Fan YC, Sun HH, Hua W, Liu HY, Wei BQ (2019) Plasmonic TiN boosting nitrogen-doped TiO_2 for ultrahigh efficient photoelectrochemical oxygen evolution. Appl Catal B-Environ 246:21–29. https://doi.org/10.1016/j.apcatb.2019.01.044

25. Liu C, Zhang C, Yin G, Zhang T, Wang W, Ou G, Jin H, Chen Z (2021) A three-dimensional branched TiO_2 photoanode with an ultrathin Al_2O_3 passivation layer and a NiOOH cocatalyst toward photoelectrochemical water oxidation. ACS Appl Mater Interfaces 13(11):13301–13310. https://doi.org/10.1021/acsami.1c00948

26. Hao J, Zhang S, Ren F, Wang Z, Lei J, Wang X, Cheng T, Li L (2017) Synthesis of TiO_2@g-C_3N_4 core-shell nanorod arrays with Z-scheme enhanced photocatalytic activity under visible light. J Colloid Interface Sci 508:419–425. https://doi.org/10.1016/j.jcis.2017.08.065

27. Liu C, Wang F, Zhang J, Wang K, Qiu Y, Liang Q, Chen Z (2018) Efficient photoelectrochemical water splitting by g-C_3N_4/TiO_2 nanotube array heterostructures. Nanomicro Lett 10(2):37–50. https://doi.org/10.1007/s40820-018-0192-6

28. Ahmad A, Tezcan F, Yerlikaya G, Zia ur R, Paksoy H, Kardaş G (2021) Three dimensional rosette-rod TiO_2/Bi_2S_3 heterojunction for enhanced photoelectrochemical water splitting. J. Alloys Compd. 868:https://doi.org/10.1016/j.jallcom.2021.159133

29. Wang J, Zhang WD (2012) Modification of TiO_2 nanorod arrays by graphite-like C_3N_4 with high visible light photoelectrochemical activity. Electrochim Acta 71:10–16. https://doi.org/10.1016/j.electacta.2012.03.102

30. Zhu L, Lu H, Hao D, Wang L, Wu Z, Wang L, Li P, Ye J (2017) Three-Dimensional Lupinus-like TiO_2 nanorod@ Sn_3O_4 nanosheet hierarchical heterostructured arrays as photoanode for enhanced photoelectrochemical performance. ACS Appl Mater Interfaces 9(44):38537–38544. https://doi.org/10.1021/acsami.7b11872

31. Lin H, Long X, An Y, Zhou D, Yang S (2019) Three-dimensional decoupling co-catalyst from a photoabsorbing

semiconductor as a new strategy to boost photoelectrochemical water splitting. Nano Lett 19(1):455–460. https://doi.org/10.1021/acs.nanolett.8b04278

32. Cho IS, Chen Z, Forman AJ, Kim DR, Rao PM, Jaramillo TF, Zheng X (2011) Branched TiO_2 nanorods for photoelectrochemical hydrogen production. Nano Lett 11(11):4978–4984. https://doi.org/10.1021/nl2029392

33. Li Z, Luo L, Li M, Chen W, Liu Y, Yang J, Xu SM, Zhou H, Ma L, Xu M, Kong X, Duan H (2021) Photoelectrocatalytic C-H halogenation over an oxygen vacancy-rich TiO_2 photoanode. Nat Commun 12(1):6698–6711. https://doi.org/10.1038/s41467-021-26997-z

34. Lin S, Ren H, Wu Z, Sun L, Zhang XG, Lin YM, Zhang KHL, Lin CJ, Tian ZQ, Li JF (2021) Direct Z-scheme WO_{3-x} nanowire-bridged TiO_2 nanorod arrays for highly efficient photoelectrochemical overall water splitting. J Energy Chem 59:721–729. https://doi.org/10.1016/j.jechem.2020.12.010

35. Yu L, Fan W, He N, Liu Y, Han X, Qin F, Ding J, Zhu G, Bai H, Shi W (2021) Effect of unsaturated coordination on photoelectrochemical properties of Ni-MOF/TiO_2 photoanode for water splitting. Int J Hydrogen Energy 46(34):17741–17750. https://doi.org/10.1016/j.ijhydene.2021.02.194

36. Chen J-J, Wu JCS, Wu PC, Tsai DP (2010) Plasmonic photocatalyst for H_2 evolution in photocatalytic water splitting. J Phys Chem C 115(1):210–216. https://doi.org/10.1021/jp1074048

37. Huo S, Wu Y, Zhao C, Yu F, Fang J, Yang Y (2020) Core–shell $TiO_2@Au_{25}/TiO_2$ nanowire arrays photoanode for efficient photoelectrochemical full water splitting. Ind Eng Chem Res 59(32):14224–14233. https://doi.org/10.1021/acs.iecr.0c02119

38. Wu F, Hu X, Fan J, Liu E, Sun T, Kang L, Hou W, Zhu C, Liu H (2012) Photocatalytic activity of Ag/TiO_2 nanotube arrays enhanced by surface plasmon resonance and application in hydrogen evolution by water splitting. Plasmonics 8(2):501–508. https://doi.org/10.1007/s11468-012-9418-5

39. Kim Woocheol, Park Jae Yeong, Kim Younghun (2019) ocatalytic reduction of Cr(VI) under visible-light irradiation. J Ind Eng Chem 73:248–253. https://doi.org/10.1016/j.jiec.2019.01.032

40. Kong W Q, Zhang X F, Guo Y Z, He G L, Liu H L, Zhang S R, Yang B C (2021) $TiO_2@PCN$ core-shell nanoarrays decorated with Au nanoparticles for enhanced photoelectrochemical performance. Electrochimica Acta 376:https://doi.org/10.1016/j.electacta.2021.138036

41. Pu YC, Wang G, Chang KD, Ling Y, Lin YK, Fitzmorris BC, Liu CM, Lu X, Tong Y, Zhang JZ, Hsu YJ, Li Y (2013) Au nanostructure-decorated TiO_2 nanowires exhibiting photoactivity across entire UV-visible region for photoelectrochemical water splitting. Nano Lett 13(8):3817–3823. https://doi.org/10.1021/nl4018385

42. Su F, Wang T, Lv R, Zhang J, Zhang P, Lu J, Gong J (2013) Dendritic Au/$TiO_{(2)}$ nanorod arrays for visible-light driven photoelectrochemical water splitting. Nanoscale 5(19):9001–9009. https://doi.org/10.1039/c3nr02766j

43. Cao Z, Yin YL, Fu P, Li D, Zhou YL, Wen ZJ, Peng YH, Wang WK, Zhou WC, Tang DS (2020) Branched TiO_2 nanorod arrays decorated with au nanostructure for plasmon-enhanced photoelectrochemical water splitting. J Electrochem Soc 167(2):026509. https://doi.org/10.1149/1945-7111/ab6a7c

44. Xu F, Mei JJ, Zheng MQ, Bai DD, Wu DP, Gao ZY, Jiang K (2017) Au nanoparticles modified branched TiO_2 nanorod array arranged with ultrathin nanorods for enhanced photoelectrochemical water splitting. J Alloys Compd 693:1124–1132. https://doi.org/10.1016/j.jallcom.2016.09.273

45. Wang X, Long R, Liu D, Yang D, Wang C, Xiong Y (2016) Enhanced full-spectrum water splitting by confining plasmonic Au nanoparticles in N-doped TiO_2 bowl nanoarrays. Nano Energy 24:87–93. https://doi.org/10.1016/j.nanoen.2016.04.013

46. Yoo J, Altomare M, Mokhtar M, Alshehri A, Al-Thabaiti SA, Mazare A, Schmuki P (2016) Photocatalytic H_2 generation using dewetted Pt-decorated TiO_2 nanotubes: optimized dewetting and oxide crystallization by a multiple annealing process. J PHYS CHEM C 120(29):15884–15892. https://doi.org/10.1021/acs.jpcc.5b12050

47. Feng M, Liu Y, Wei N, Ma S, Li Z, Li H, Chen S, Liu J, Wang D (2018) Alumina anchored CQDs/TiO_2 nanorods by atomic layer deposition for efficient photoelectrochemical water splitting under solar light. J Mater Chem A 6(37):18293–18303. https://doi.org/10.1039/c8ta05092a

48. Shuang S, Zhang Z (2018) The effect of annealing treatment and atom layer deposition to Au/Pt nanoparticles-decorated $TiO_{(2)}$ nanorods as photocatalysts. Molecules 23(3):525–536. https://doi.org/10.3390/molecules23030525

49. Altomare M, Nguyen NT, Hejazi S, Schmuki P (2018) A cocatalytic electron-transfer cascade site-selectively placed on TiO_2 nanotubes yields enhanced photocatalytic H_2 evolution. Adv Funct Mater 28(2):1704259. https://doi.org/10.1002/adfm.201704259

50. Cai Y, Yuan F, Li F, Kang H, Xue D, Huo S, Yu F, Fang J, Yang Y (2021) Spacing prior to decorating TiO_2 nanowires with dewetted Au nanoparticles for boosting photoelectrochemical water oxidation. CrystEngComm 23(37):6551–6558. https://doi.org/10.1039/d1ce00886b

51. Zhang X, Liu Y, Kang Z (2014) 3D branched ZnO nanowire arrays decorated with plasmonic au nanoparticles for high-performance photoelectrochemical water splitting. ACS Appl Mater Interfaces 6(6):4480–4490. https://doi.org/10.1021/am500234v

52. Dou YB, Zhou J, Zhou A, Li JR, Nie ZR (2017) Visible-light responsive MOF encapsulation of noble-metal-sensitized semiconductors for high-performance photoelectrochemical water splitting. J Mater Chem A 5(36):19491–19498. https://doi.org/10.1039/c7ta06443h

53. Yang W, Yu Y, Starr MB, Yin X, Li Z, Kvit A, Wang S, Zhao P, Wang X (2015) Ferroelectric polarization-enhanced photoelectrochemical water splitting in TiO_2-$BaTiO_3$ core-shell nanowire photoanodes. Nano Lett 15(11):7574–7580. https://doi.org/10.1021/acs.nanolett.5b03988

54. Li J, Cushing SK, Zheng P, Meng F, Chu D, Wu N (2013) Plasmon-induced photonic and energy-transfer

enhancement of solar water splitting by a hematite nanorod array. Nat Commun 4(1):2651–2659. https://doi.org/10.1038/ncomms3651

55. Zhang Z, Zhang L, Hedhili MN, Zhang H, Wang P (2013) Plasmonic gold nanocrystals coupled with photonic crystal seamlessly on TiO2 nanotube photoelectrodes for efficient visible light photoelectrochemical water splitting. Nano Lett 13(1):14–20. https://doi.org/10.1021/nl3029202

56. Warren SC, Thimsen E (2012) Plasmonic solar water splitting. Energy Environ Sci 5(1):5133–5146. https://doi.org/10.1039/c1ee02875h